

# Supporting Information

## Metal Sputtering Buffer Layer for High Performance

### Si-based Water-oxidation Photoanode

*Chang Zhao<sup>†,‡,#</sup>, Beidou Guo<sup>†,‡,#</sup>, Guancai Xie<sup>†,‡</sup>, Chengcheng Li<sup>§</sup>, Wenjing Xie<sup>†</sup>, Yawen Dai<sup>†,‡</sup>, Jinlong Gong<sup>§,\*</sup>, and Jian Ru Gong<sup>†,\*</sup>*

<sup>†</sup>Chinese Academy of Sciences (CAS) Center for Excellence in Nanoscience, CAS Key Laboratory of Nanosystem and Hierarchy Fabrication, National Center for Nanoscience and Technology, Beijing, 100190, P. R. China

<sup>‡</sup> University of CAS, Beijing 100049, P. R. China

<sup>§</sup> Key Laboratory for Green Chemical Technology of Ministry of Education, School of Chemical Engineering and Technology, Tianjin University; Collaborative Innovation Center of Chemical Science and Engineering, Tianjin 300072, P. R. China

Corresponding emails: gongjr@nanoctr.cn

jlgong@tju.edu.cn

## Table of Contents

Experimental Section .....	S2
Results and Discussion.....	S10
References .....	S23

## Experimental Section

### Materials and chemicals

The commercial phosphorus-doped monocrystalline Si (n-type, single-side polished, (100)-oriented, resistivity 0.1–0.9  $\Omega$  cm, 525 mm) was purchased from Zhejiang Lijing Technology Co., Ltd. Ultrapure water (resistivity = 18 M $\Omega$  cm) that used for preparing all solutions was obtained from a Milli-Q system. The ethanol (AR,  $\geq$  99.8%) and isopropyl alcohol (AR,  $\geq$  99.7%) were purchased from Beijing Chemical Works. The nickel nitrate ( $\text{Ni}(\text{NO}_3)_2 \cdot 6\text{H}_2\text{O}$ , 99.999%, Guanhua Sci-Tech Co., Ltd), iron sulfate ( $\text{FeSO}_4 \cdot 7\text{H}_2\text{O}$ , (99.999 %, Xilong Scientific Co., Ltd.), and KOH (82%, Beijing Chemical Works) were used as received without further treatment. The Ni and NiFe alloy target (diameter 50.8 mm, Zhongnuo Advanced Materials (Beijing)Technology Co., Ltd).

### Preparation of photoanodes

The commercial phosphorus-doped monocrystalline Si was cleaved into pieces of dimension 1 cm  $\times$  1 cm. These Si pieces were first cleaned for 30 min successively in acetone, isopropanol alcohol and deionized water by ultrasonication and then dried by blowing  $\text{N}_2$ . The Si wafers were then immersed in buffered HF solutions (2%) for 2 min to completely

remove the native oxide layer on the Si surface and the residual HF was rinsed off with water. After drying under N<sub>2</sub> gas, the Si wafers were quickly transferred to the atomic layer deposition (ALD) chamber.

The Al<sub>2</sub>O<sub>3</sub> film was deposited on the etched Si wafers at 200 °C using trimethylaluminum (TMA) as the Al source, deionized water vapor as the oxygen source and N<sub>2</sub> as the carrier gas. Each ALD cycle included 15 ms pulse of TMA, 15 s N<sub>2</sub> purge, 15 ms deionized water pulse, and 15 s N<sub>2</sub> purge. The thickness of Al<sub>2</sub>O<sub>3</sub> was controlled by changing the number of cycles. 25 cycles were necessary to deposit ~2.2 nm of Al<sub>2</sub>O<sub>3</sub> and the film thickness was confirmed by cross-sectional high-resolution transmission electron microscopy and energy dispersive spectroscopy mapping.

Prior to the deposition of NiFeO<sub>x</sub>, a 2 nm-thick Ni film was deposited on the Si/Al<sub>2</sub>O<sub>3</sub> substrate by thermal evaporation. The Si/Al<sub>2</sub>O<sub>3</sub>/Ni substrate was then transferred to a high vacuum magnetron sputtering chamber. NiFeO<sub>x</sub> film was deposited on the substrate by radio frequency (RF) reactive magnetron sputtering using NiFe alloy as the target. The content of Fe in NiFeO<sub>x</sub> was adjusted by changing the Ni/Fe ratio in the target. It is common to heat the substrate when preparing the Ni-based oxide, of which 300 °C is the often used preparation temperature.<sup>1</sup> Moreover, the effect of the deposition temperature on the performance of the prepared NiO<sub>x</sub> film has been studied.<sup>2</sup> It has been found that the conductivity of the photoelectrode with NiO<sub>x</sub> coatings deposited under high temperatures shows no significant change after activation. Whereas the same samples deposited without heating of the substrate showed a reduced slope at positive bias after activation, which is harmful to the PEC performance. Therefore, the substrate temperature was maintained at 300 °C with background pressure <4×10<sup>-4</sup> Pa before deposition. During sputtering, the ratio of O<sub>2</sub> to Ar was 1:10, and the sputtering pressure and RF sputtering power were 0.2 Pa and 80 W, respectively. The time taken to deposit ~57 nm NiFeO<sub>x</sub> was 15 min. The back contact for the n-Si is ohmic

contact, which was formed by scratching the back side of the Si substrate to remove the surface oxide, followed by applying In-Ga alloy and contacting with a Cu wire. The exposed areas of all the photoanodes were measured using ImageJ software and were 0.15-0.3 cm<sup>2</sup> unless specified otherwise.

The NiFe-layered double hydroxide (LDH) was electrodeposited in a three-electrode configuration, by using the as-prepared Si/Al<sub>2</sub>O<sub>3</sub>/Ni/NiFeO<sub>x</sub>, Pt net and a saturated calomel electrode (SCE) as the working, counter, and reference electrodes. The electrolyte was prepared by dissolving Ni(NO<sub>3</sub>)<sub>2</sub>·6H<sub>2</sub>O (0.15 M) and FeSO<sub>4</sub>·7H<sub>2</sub>O (0.15 M) in 70 mL water under stirring in inert Ar gas atmosphere, to prevent the self-oxidation of Fe<sup>2+</sup> into Fe<sup>3+</sup>. The applied potential was -1 V vs. SCE and the electrodeposition time was 30 s.

## **Characterization**

Scanning electron microscopy (SEM) images were obtained using an ultrahigh resolution cold field emission scanning electron microscope (Hitachi-SU8220) at the accelerating voltage of 10 kV. Atomic force microscopy (AFM) images were collected with a Bruker Dimension Icon operating in lateral force microscopy mode using Bruker ScanAsyst-Air probes (silicon tip; silicon nitride cantilever, spring constant: 0.4 N m<sup>-1</sup>, frequency: 70 KHz) and analyzed using NanoScope Analyst software (version 1.40). The ultraviolet-visible (UV-vis) transmittance (T) and reflectance (R) spectra were obtained using a UV-vis spectrophotometer (UV-2600) equipped with an integrating sphere. The absorbance (A) was calculated by the formula  $A = 1 - T - R$ . X-ray photoelectron spectroscopy (XPS) was performed in an ultrahigh vacuum system equipped with a monochromatic Al K $\alpha$  (1486.6 eV) source (ESCALAB250Xi). High-resolution transmission electron microscopy (HRTEM) images and energy-dispersive spectroscopy (EDS) mapping were carried out in a field-emission transmission electron microscope (Titan Cubed Themis G2 300) operated at 200 kV and equipped with a high-brightness field emission gun (X-FEG), a monochromator unit, a

probe and image spherical aberration (Cs) corrector, and a super-X EDXS system. The solid-state experiments measurements were carried out in the dark on a probe station (Lakeshore, TTP4) equipped with a semiconductor characterization system (Keithley 4200) in air. As for the tested Si/Al<sub>2</sub>O<sub>3</sub>/Ni/NiFeO<sub>x</sub> and Si/Al<sub>2</sub>O<sub>3</sub>/NiFeO<sub>x</sub> samples, one side was connected to the lead wire and another side was connected with probe.

### Electrochemical measurements

Electrochemical measurements were performed using a standard three-electrode system on a Zahner Zennium electrochemical workstation with the prepared photoanode as the working electrode, a Pt sheet as the counter electrode, and an SCE as the reference electrode under simulated AM 1.5G sunlight (100 mW cm<sup>-2</sup>) irradiation generated from a 500 W Xenon lamp equipped with an AM 1.5G filter (CEL-S500, Aulight, Beijing, China). The light was illuminated from the front side (the side of electrocatalyst deposition) for all measurements under light irradiation. The ferri/ferrocyanide solution concentration was adjusted to be 5 mM of both K<sub>3</sub>Fe(CN)<sub>6</sub> and K<sub>4</sub>Fe(CN)<sub>6</sub>·3H<sub>2</sub>O in 1 M aqueous KCl. 1 M KOH was the electrolyte with stirred and unsaturated with oxygen in photoelectrochemical water oxidation tests. Cyclic voltammetry (C-V) curves were recorded after 30 cycles of activation at the scan rate of 100 mV s<sup>-1</sup>. The current density-time dependent stability test was performed at 0.66 V vs. SCE in 1 M KOH under simulated AM 1.5G solar irradiation.

The measured potential vs. SCE was converted to that with reference to a reversible hydrogen electrode (RHE) using the following equation:

$$E_{RHE} = E_{SCE} + 0.244 + 0.059 \times pH \quad (S1)$$

where  $E_{RHE}$  is the potential vs. RHE,  $E_{SCE}$  is the potential vs. SCE, and 0.244 is the standard potential of the SCE.

### Applied bias photon-to-current efficiency (ABPE)

Assuming 100% Faradic efficiency for the oxidation of water to O<sub>2</sub>, the ABPE of the Si/Al<sub>2</sub>O<sub>3</sub>/Ni/NiFeO<sub>x</sub> was calculated from the current density vs. potential curves using the following equation:

$$ABPE = \frac{J \times (1.23 - E_{bias})}{P_{in}} \times 100\% \quad (S2)$$

where  $J$  is the current density (mA cm<sup>-2</sup>),  $E_{bias}$  is the externally applied bias vs. RHE, and  $P_{in}$  is the irradiance intensity, which is 100 W cm<sup>-2</sup>.

### Photovoltage test

The magnitude of photovoltage was confirmed from the difference in the electrochemical open-circuit potential (OCP) values measured in the dark and under irradiation. The OCP was measured in 1M KOH electrolyte in the three-electrode system in the dark and under AM 1.5G simulated sunlight irradiation at zero current density. All the OCP readings were obtained after half an hour of stabilization. The photovoltage ( $V_{ph}$ ) was calculated according to the following equation:

$$V_{ph} = |OCP_{light} - OCP_{dark}| \quad (S3)$$

where  $OCP_{light}$  is the OCP measured under AM1.5G simulated sunlight irradiation, and  $OCP_{dark}$  is the OCP measured in the dark.

### Electrochemical impedance spectroscopy (EIS)

EIS was performed at the potential of 1.03 V<sub>RHE</sub> for Si/Al<sub>2</sub>O<sub>3</sub>/Ni/NiFeO<sub>x</sub> and Si/Al<sub>2</sub>O<sub>3</sub>/NiFeO<sub>x</sub> photoanodes in the frequency range from 1 Hz to 1 MHz with an AC amplitude of 10 mV under AM 1.5G irradiation. The EIS plot was analyzed by fitting with the equivalent circuit diagrams using ZsimpWin software. Due to the geometrical factors of the electrode surface (porous, rough, etc.) and the presence of adsorption, the part of the electrode process that represents the nature of the pure capacitance will deviate from the pure

capacitance in the actual process. In this case, it is difficult to give a satisfactory fitting result with pure capacitance in the equivalent circuit, and thus a constant phase element (CPE) is provided to replace purely capacitive components to fit the required settings. The equivalent circuit model includes the system resistance  $R_s$ , the bulk charge transfer resistance ( $R_1$ ), the Si photoanode-electrolyte interface charge transfer resistance ( $R_2$ ), and the two constant phase elements (CPE1 and CPE2).<sup>4-5</sup> The semicircle in the high-frequency region corresponds to the charge transfer process in the bulk and the semicircle in the low-frequency region corresponds to the charge transfer process at the interface between the electrodes and the electrolyte. For the Si/Al<sub>2</sub>O<sub>3</sub>/Ni/NiFeO<sub>x</sub> photoanode,  $R_1$  and  $R_2$  are 11 and 39  $\Omega$ , respectively, which are smaller than those of the photoanode without Ni film.

### Mott-Schottky (MS) analysis

To calculate the flat-band potential of the photoanode, we tested the EIS over a range of frequencies at different potentials and fitting to an appropriate circuit. MS plots were traced in the dark in contact with 10 mM K<sub>3</sub>Fe(CN)<sub>6</sub>, 10 mM K<sub>4</sub>Fe(CN)<sub>6</sub>·3H<sub>2</sub>O and 1 M KCl.<sup>1,6</sup> The three electrode measurement was used with a Pt wire as the reference electrode and a Pt coil as the counter electrode. The fluctuation voltage was set to 5 mV rms. The potentiostatic EIS measurements were performed at 0.1 V intervals between 0.5 – 0.8 V versus Fe(CN)<sub>6</sub><sup>3-/4-</sup> with a frequency range of 3000–200000 Hz.<sup>7</sup> The equivalent circuit model is same as that used in Figure 5a. The reverse-bias-dependent differential capacitance-potential in the depletion layer of Si/Al<sub>2</sub>O<sub>3</sub>/Ni/NiFeO<sub>x</sub> (and of Si/Al<sub>2</sub>O<sub>3</sub>/NiFeO<sub>x</sub>) is related to the Mott-Schottky relation:

$$\frac{1}{C^2} = \frac{2}{A^2 \epsilon_0 \epsilon_r q N_D} \left( V - E_{fb} - \frac{k_B T}{q} \right) \quad (S4)$$

where  $A$  is the area of the photoanode,  $C$  is the differential capacitance,  $\epsilon_0$  is the permittivity of vacuum,  $\epsilon_r$  is the relative permittivity,  $q$  is the charge of an electron ( $1.6 \times 10^{-19}$  C),  $N_D$  is the donor concentration of the semiconductor,  $V$  is the external bias,  $k_B$  is the Boltzmann

constant ( $1.38 \times 10^{-23}$  J/K),  $T$  is the room temperature (298 K), and  $E_{fb}$  is the flat band potential estimated from the MS plot. For the Si/Al<sub>2</sub>O<sub>3</sub>/Ni/NiFeO<sub>x</sub> and Si/Al<sub>2</sub>O<sub>3</sub>/NiFeO<sub>x</sub> photoanodes, the  $E_{fb}$  values were calculated to be, respectively, -0.88 and -0.5 V vs. Fe(CN)<sub>6</sub><sup>3-/4-</sup>.

The barrier height  $\phi_b$  can then be calculated using the following formula:

$$\phi_b = E_{fb} + V_n \quad (S5)$$

$$V_n = k_B T \ln \left( \frac{N_c}{N_D} \right) \quad (S6)$$

$V_n$  is the difference between the potential of the Fermi level and the conduction band edge, and  $N_c$  is the density of conduction band states. The Mott-Schottky plots of the Si/Al<sub>2</sub>O<sub>3</sub>/Ni/NiFeO<sub>x</sub> and Si/Al<sub>2</sub>O<sub>3</sub>/NiFeO<sub>x</sub> photoanode (Figure 6a) display that their slope is  $(1.6 \pm 0.2) \times 10^{14}$ . According to the equation S4, the donor concentration of the semiconductor ( $N_D$ ) was calculated to be  $(7.5 \pm 1) \times 10^{16}$  cm<sup>-3</sup>, corresponding a resistivity of about 0.1  $\Omega$  cm for the n-Si wafer, which is in accordance with the range of 0.1–0.9  $\Omega$  cm provided by the manufacturer.<sup>1</sup> On the basis of the  $N_D$ , equation S5 and S6, the  $V_n$  was calculated to be 0.15 eV, and the barrier height values for the Si/Al<sub>2</sub>O<sub>3</sub>/Ni/NiFeO<sub>x</sub> and Si/Al<sub>2</sub>O<sub>3</sub>/NiFeO<sub>x</sub> photoanodes, were calculated to be, 1.03 and 0.65 eV vs. Fe(CN)<sub>6</sub><sup>3-/4-</sup>, respectively. In Figure 6a, the measured 4 data points for the Mott Schottky plots show a favorable linear relationship with a fitted correlation coefficient  $R^2$  of more than 0.99.<sup>8</sup> It thus can be sure that the Mott Schottky plots based on the 4 data points are also credible.

### **The Relationship between photovoltage ( $V_{ph}$ ) and barrier height ( $\phi_b$ )**

The  $j_s$  can be calculated from the dark saturation current using the following formula<sup>9-11</sup>:

$$j_s = A^* T^2 \exp \left( \frac{-q\phi_b}{kT} \right) \exp \left( -\sqrt{\chi} \delta \right) \quad (S7)$$

The  $V_{ph}$  can be described using the following formula<sup>10</sup>:

$$V_{ph} = \frac{nkT}{q} \ln \left( \frac{j_L}{j_s} \right) \quad (S8)$$



Combining Equation (S7) and (S8), the following relationship is given as:

$$V_{ph} = \frac{nkT}{q} \left[ \ln \left( \frac{J_L}{A^* T^2} \right) + \frac{q\phi_b}{kT} + \sqrt{\chi} \delta \right] \quad (S9)$$

where  $n$  is the diode quality factor,  $k$  is the Boltzmann constant ( $1.38 \times 10^{-23}$  J/K),  $T$  is the room temperature (298 K),  $q$  is the charge of an electron ( $1.6 \times 10^{-19}$  C),  $J_L$  is the light-limited current density ( $A\ cm^{-2}$ ),  $A^*$  is the effective Richardson's constant,  $\chi$  (in eV) is the mean barrier height presented by the tunnel oxide and  $\delta$  is the thickness of the tunnel oxide. According to Equation S9, the  $V_{ph}$  is positively related to  $n$ ,  $J_L$  and  $\phi_b$  as all the other parameters are constants for our n-Si based photoanode.

### Charge separation and injection efficiency

H<sub>2</sub>O<sub>2</sub>, a hole scavenger (assuming 100% injection efficiency) was introduced into the electrolyte.<sup>5-6</sup> The current density-voltage curves in 1M KOH and 1M KOH + 0.5 M H<sub>2</sub>O<sub>2</sub> were used to determine  $\eta_{sep}$  and  $\eta_{inj}$  according to the following equation<sup>12</sup>:

$$\eta_{sep} = \frac{J_{H_2O_2}}{J_{abs}} \quad (S10)$$

$$\eta_{inj} = \frac{J_{H_2O}}{J_{H_2O_2}} \quad (S11)$$

where  $J_{H_2O_2}$  is the photocurrent density in 1 M KOH + 0.5 M H<sub>2</sub>O<sub>2</sub>,  $J_{H_2O}$  is the photocurrent density for water oxidation in 1M KOH, and  $J_{abs}$  is the calculated photocurrent density when the absorbed photons are completely transformed to current.

### Width of space charge region

The width of the space charge region ( $W$ ) can be described by the following equation:

$$W = \sqrt{\frac{2\epsilon_r \epsilon_0 V_{bi}}{qN_D}} \quad (S12)$$

where  $q$  is the electron charge,  $\epsilon_r$  is the dielectric constant of Si,  $\epsilon_0$  is the permittivity of vacuum,  $N_D$  is the carrier density, and  $V_{bi}$  is the built-in potential. As depicted in equation

S12,  $W$  is directly related to  $V_{bi}$  as all the other parameters are constants for an n-Si based photoanode. Since the built-in potential increases as the barrier height increases from 0.65 to 1.03 eV following the inclusion of a Ni film, there is a corresponding increase in the width of the space charge region.

## Results and Discussion

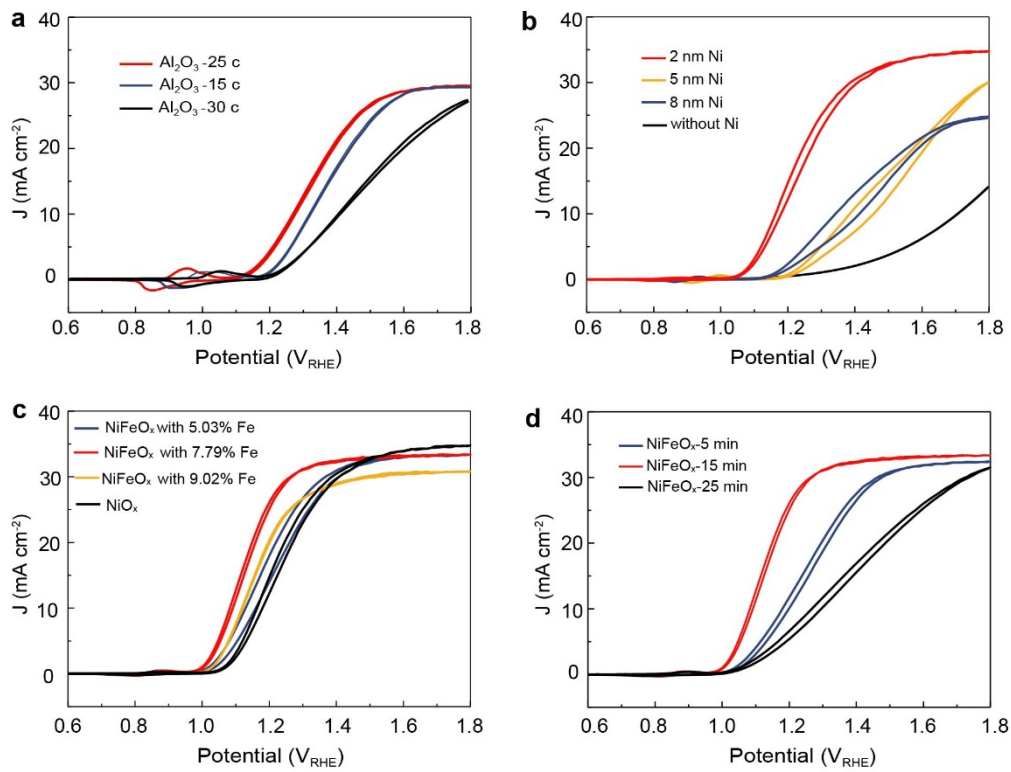


**Figure S1.** PEC performance optimization of the anodes. (a) J-V curves of the Si/Al<sub>2</sub>O<sub>3</sub>/Ni anodes with different Al<sub>2</sub>O<sub>3</sub> thicknesses. (b) J-V curves of the Si/Al<sub>2</sub>O<sub>3</sub>/Ni/NiO<sub>x</sub> with different thickness of Ni film. (c) J-V curves of the Si/Al<sub>2</sub>O<sub>3</sub>/Ni/NiFeO<sub>x</sub> deposited using the sputtering target with different Ni/Fe ratios. (d) J-V curves of the Si/Al<sub>2</sub>O<sub>3</sub>/Ni/NiFeO<sub>x</sub> with different sputtering times for NiFeO<sub>x</sub>.

To optimize PEC performance, the thickness of Al<sub>2</sub>O<sub>3</sub>, Ni, NiFeO<sub>x</sub> and the content of Fe in NiFeO<sub>x</sub> were optimized. First, to optimize the thickness of Al<sub>2</sub>O<sub>3</sub>, Si/Al<sub>2</sub>O<sub>3</sub>/Ni photoanodes with 5 nm Ni and different thickness of Al<sub>2</sub>O<sub>3</sub> were prepared. The thickness of Al<sub>2</sub>O<sub>3</sub> was controlled by changing the number of ALD cycles. It is clearly seen from Figure S1a that the photoanode with 25 cycles of Al<sub>2</sub>O<sub>3</sub> shows the lowest onset potential among the three samples. Next, the thickness of the Ni interlayer was adjusted by fixing the thickness of Al<sub>2</sub>O<sub>3</sub> film at the optimal value (25 cycles) and that of the NiO<sub>x</sub> film to be ~50 nm in the Si/Al<sub>2</sub>O<sub>3</sub>/Ni/NiO<sub>x</sub> photoanodes (Figure S1b). With increasing thickness of Ni, the saturation photocurrents of the photoanodes decrease due to reduced light transmission and Si/Al<sub>2</sub>O<sub>3</sub>/Ni/NiO<sub>x</sub> with 2 nm Ni shows the best PEC performance. Subsequently, we adjusted the content of Fe in the Si/Al<sub>2</sub>O<sub>3</sub>/Ni/NiFeO<sub>x</sub> with a fixed thickness of Al<sub>2</sub>O<sub>3</sub> film (25 cycles), Ni film (2 nm) and NiFeO<sub>x</sub> (55 ± 5 nm) by changing the ratio of Ni and Fe in the sputtering target. The content of Fe in NiFeO<sub>x</sub> was confirmed by XPS analysis (Figure S2). As depicted in Figure S1c, the Si/Al<sub>2</sub>O<sub>3</sub>/Ni/NiFeO<sub>x</sub> photoanode with 7.79% Fe shows the best PEC performance among the different samples. Finally, the thickness of NiFeO<sub>x</sub> was optimized by changing the sputtering time from 5 to 25 min at 10 min intervals and keeping other parameters constant at their optimal values. As the thickness of the electrocatalyst increases, both of the depletion layer of Si and series resistance loss of the electrocatalyst increase<sup>13</sup>. The increased depletion layer of Si is conducive to the charge separation, which is beneficial to the PEC performance; while the series resistance loss causes the PEC performance degradation. Therefore, there is a trade-off between increased depletion of Si and series resistance loss for thick electrocatalysts. To acquire high PEC performance, an optimum thickness configuration should be expected to balance this trade-off. Therefore, we deposited NiFeO<sub>x</sub> with different thicknesses by changing the deposition time and investigated its effect for PEC performance. As shown in Figure S1d, the onset potential decreased and then increased with the deposition time increased from 5 to 25 min. In the

case of 5-min deposition for thin  $\text{NiFeO}_x$ , an inferior PEC performance was observed due to the increased charge recombination caused by narrow depletion layer, although the series resistance loss is low. In the case of 25-min deposition for thick  $\text{NiFeO}_x$ , the large series resistance loss is harmful to the PEC performance. Therefore, an optimum thickness of 15-min deposition is expected to balance the trade-off between depletion of Si and series resistance, thus leading to the best PEC performance.

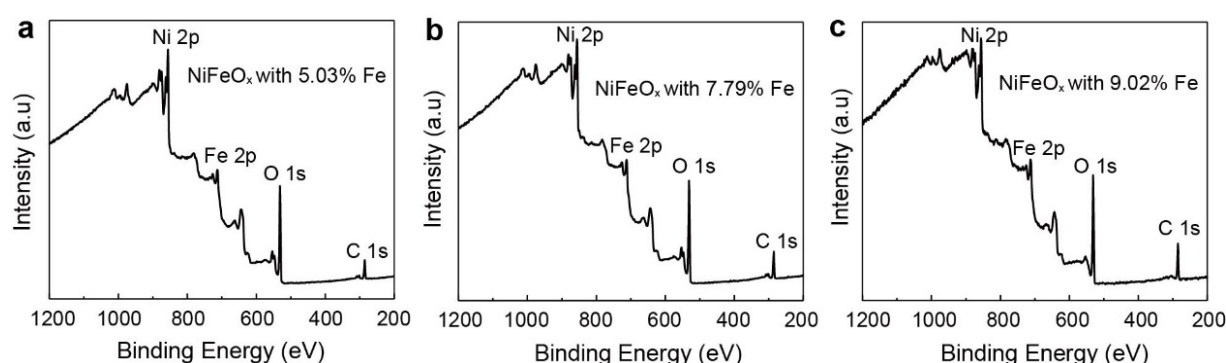


**Figure S2.** XPS survey spectrum of  $\text{Si}/\text{Al}_2\text{O}_3/\text{Ni}/\text{NiFeO}_x$  photoanode with the Fe mass percentage of (a) 5.03%, (b) 7.79% and (c) 9.02%.

The content of Fe in the  $\text{NiFeO}_x$  film was altered by simply changing the Ni/Fe ratio in the sputtering target. The final content was confirmed by calculating the mass percentage of Fe in all elements from XPS spectral data. As for the  $\text{NiFeO}_x$  film prepared by using the sputtering targets with the Ni/Fe atomic ratio of 8:2, the mass percentages of Ni, Fe and O are 35.74%, 7.79% and 56.47%. Since the bombarding degree of difficulty of each element in the alloy target are different, the element ratio in the product is usually different from that in the target. In our prepared  $\text{NiFeO}_x$  film, Ni element is more likely to be bombarded out to participate in the reaction, while Fe element is more likely to remain in the target material because it is more difficult to be bombarded. Therefore, the ratio of Fe in the  $\text{NiFeO}_x$  film is lower than that in the NiFe alloy target.

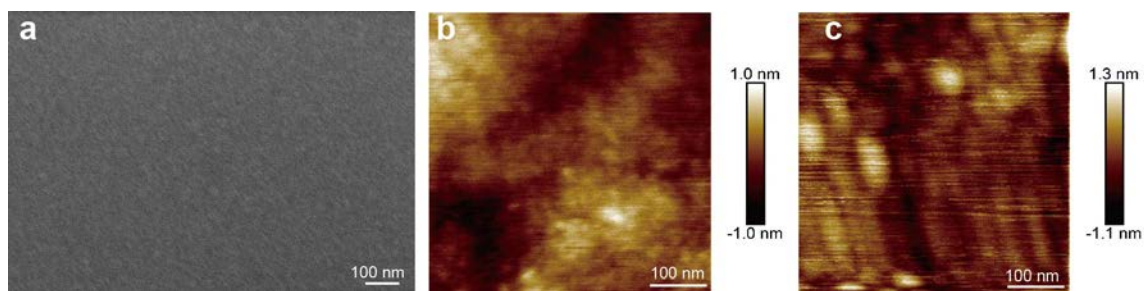


**Figure S3.** (a) SEM and (b) AFM images of the Si/Al<sub>2</sub>O<sub>3</sub>/Ni/NiFeO<sub>x</sub>. (c) AFM image of the Si/Al<sub>2</sub>O<sub>3</sub>/NiFeO<sub>x</sub>.

The surface roughness of these two electrodes are 0.235 and 0.257 nm respectively and the difference between them is negligible, indicating that the NiFeO<sub>x</sub> exhibits similar roughness for these two electrodes. This result proves that the surface roughness is not the main cause of the overpotential change for these two electrodes.

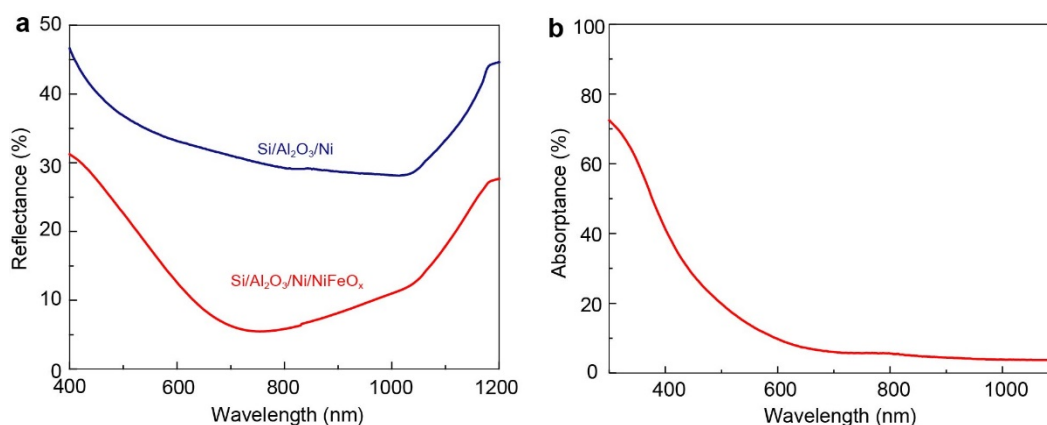


**Figure S4.** (a) UV-vis reflectance spectra of the Si/Al<sub>2</sub>O<sub>3</sub>/Ni/NiFeO<sub>x</sub> and Si/Al<sub>2</sub>O<sub>3</sub>/Ni photoanodes. (b) UV-vis absorbance spectrum of the NiFeO<sub>x</sub> film deposited on a quartz glass substrate.

The UV-vis reflectance spectra of the Si/Al<sub>2</sub>O<sub>3</sub>/Ni/NiFeO<sub>x</sub> and bare Si photoanodes were traced (Figure S4a). Compared to the Si/Al<sub>2</sub>O<sub>3</sub>/Ni photoanode, the Si/Al<sub>2</sub>O<sub>3</sub>/Ni/NiFeO<sub>x</sub> photoanode shows reduced light reflection in the entire wavelength range, demonstrating the effective anti-reflection property of the NiFeO<sub>x</sub> film.<sup>14</sup> The absorption of the NiFeO<sub>x</sub> film is

in the spectral range of wavelength  $<600$  nm (Figure S4b). For the spectral range of wavelength  $>600$  nm, the absorption of the  $\text{NiFeO}_x$  film is near zero, indicating thereby, good light transmission. This result shows that the  $\text{NiFeO}_x$  film has high transmittance.

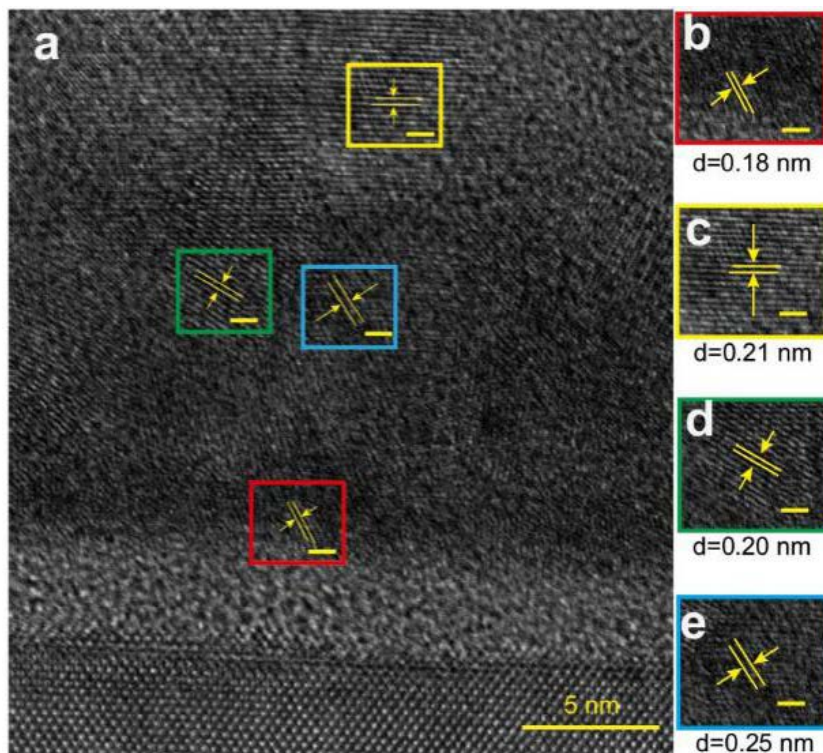


**Figure S5.** (a) Cross-sectional HRTEM image of the  $\text{Si}/\text{Al}_2\text{O}_3/\text{Ni}/\text{NiFeO}_x$  photoanode after 30 C-V cycles of activation. (b) the zoomed-in HRTEM images of selected areas of Ni film. (c,d,e) the zoomed-in HRTEM images of selected areas of  $\text{NiFeO}_x$  film (Scale bars: 1 nm).

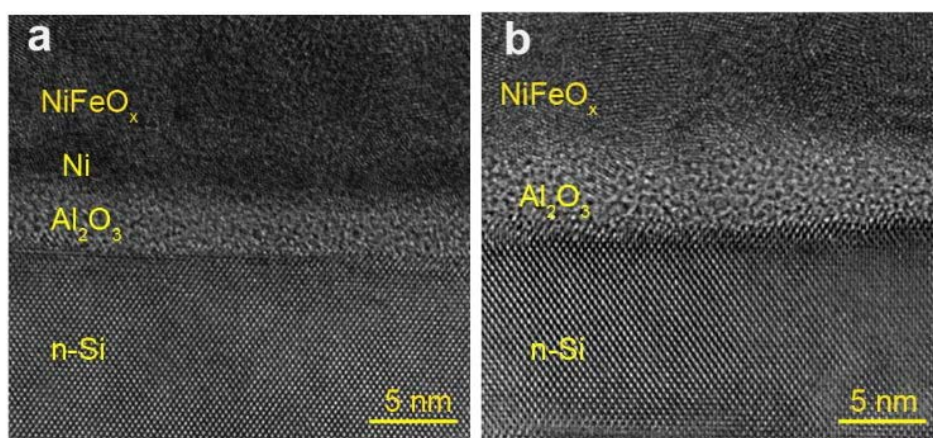


**Figure S6.** The raw images of the (a) Figure 2a and (b) Figure 2c.



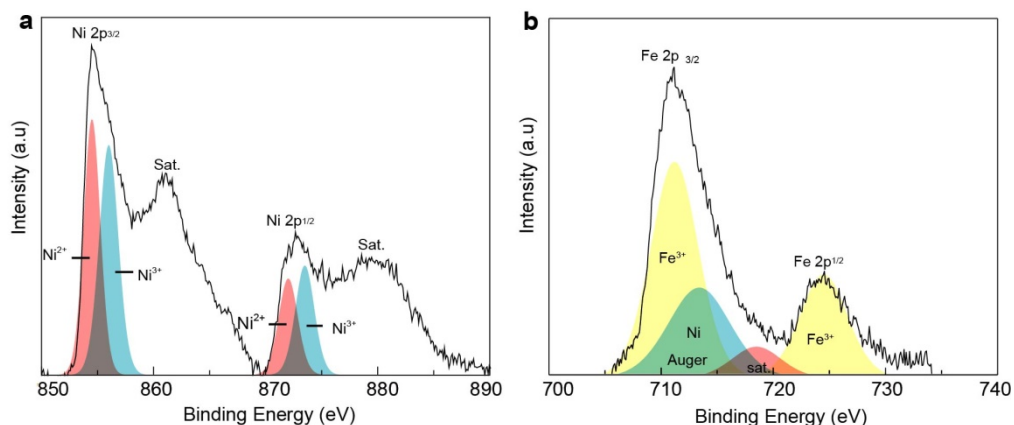


**Figure S7.** (a) Ni 2p and (b) Fe 2p XPS spectra of the Si/Al<sub>2</sub>O<sub>3</sub>/Ni/NiFeO<sub>x</sub> photoanode.

XPS was performed to reveal the chemical states of the different elements in sputtered NiFeO<sub>x</sub>. As shown in Figure S7a, both Ni<sup>(II)</sup> (pink color) and the Ni<sup>(III)</sup> (blue color) corresponding to NiO and Ni<sub>2</sub>O<sub>3</sub>, respectively, are present in the Ni XPS spectrum.<sup>15-16</sup> The peaks at 711.0 and 724.5 eV in the Fe 2p spectrum (Figure S7b) are assigned to Fe (2p<sub>3/2</sub>) and Fe (2p<sub>1/2</sub>) of Fe<sup>(III)</sup><sup>16-17</sup> and the peak at 713.4 eV is assigned to the Auger peak of Ni.<sup>18-20</sup> These results indicate that both Ni and Fe are in their oxidized form, confirming the formation of NiFe oxide film.

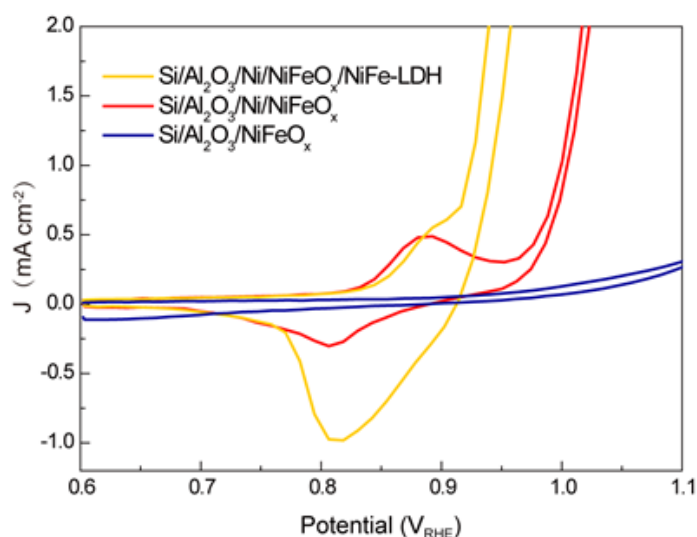


**Figure S8.** The magnification of the J-V curves for the Si/Al<sub>2</sub>O<sub>3</sub>/Ni/NiFeO<sub>x</sub>, Si/Al<sub>2</sub>O<sub>3</sub>/Ni/NiFeO<sub>x</sub> and Si/Al<sub>2</sub>O<sub>3</sub>/Ni/NiFeO<sub>x</sub>-LDH photoanodes.

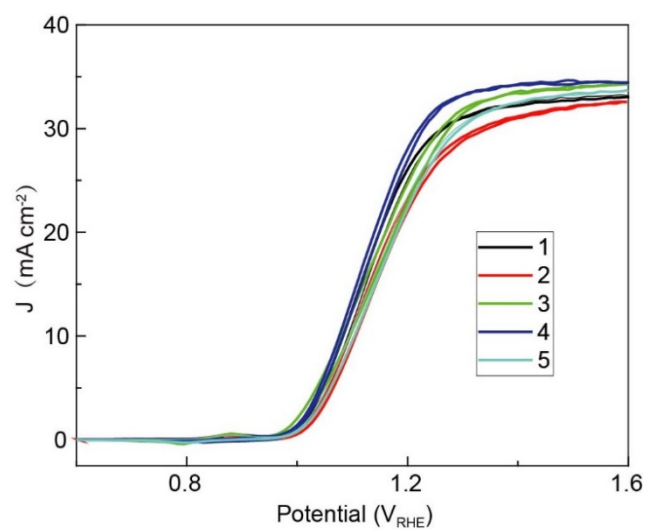


**Figure S9.** The J-V curves of the 5 Si/Al<sub>2</sub>O<sub>3</sub>/Ni/NiFeO<sub>x</sub> photoanodes.

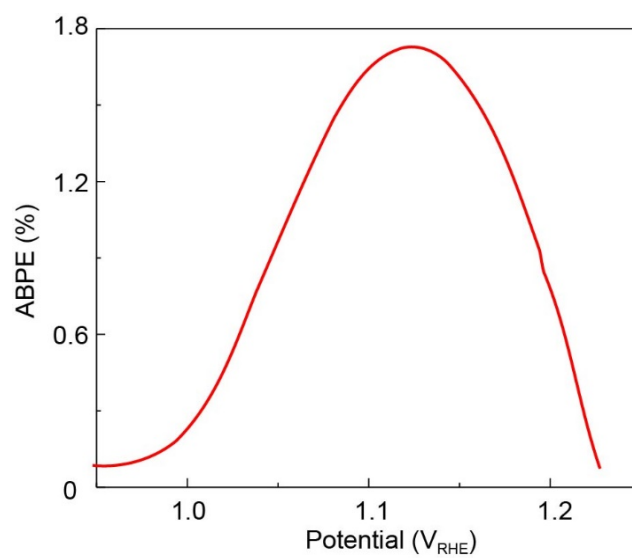


**Figure S10.** ABPE of the Si/Al<sub>2</sub>O<sub>3</sub>/Ni/NiFeO<sub>x</sub> photoanode.



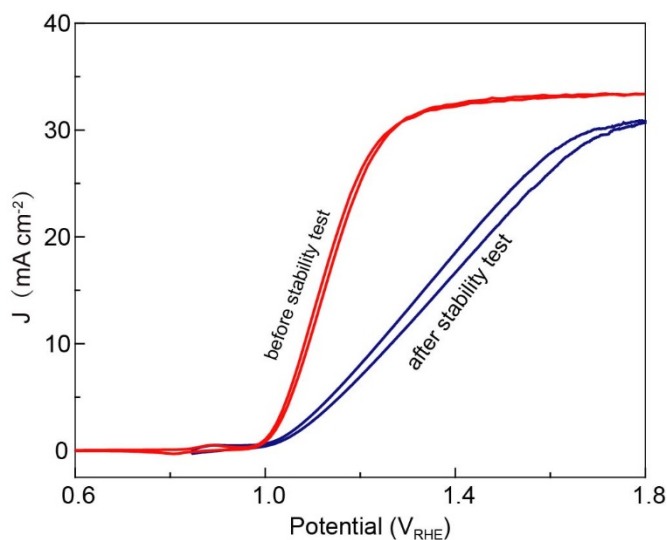


**Figure S11.** The J-V curves of the Si/Al<sub>2</sub>O<sub>3</sub>/Ni/NiFeO<sub>x</sub> photoanode before and after stability test.

As shown in Figure S11, the saturated photocurrent densities of the Si/Al<sub>2</sub>O<sub>3</sub>/Ni/NiFeO<sub>x</sub> photoanode at 1.7 V<sub>RHE</sub> before and after the stability test show no obvious change, suggesting no catastrophic failure.<sup>21</sup> However, the fill factor shows a decrease after the stability test compared to that before the stability test.<sup>22</sup> The decrease of the fill factor might be caused by the formation of a SiO<sub>x</sub> layer on the Si surface due to the pinholes generated in the NiFeO<sub>x</sub> film during the long-term operation, causing an increase in tunneling resistivity arising from the increase of the thickness of the SiO<sub>x</sub> layer at the interface.<sup>1,23</sup>

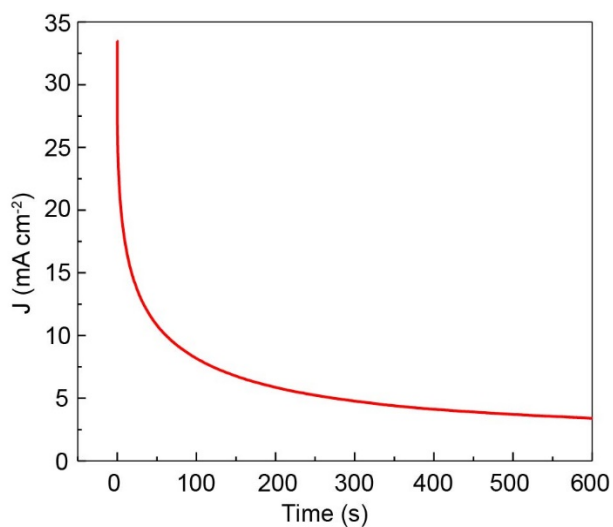


**Figure S12.** Chronoamperometric curve of the Si/Al<sub>2</sub>O<sub>3</sub>/Ni photoanode measured at 1.7 V<sub>RHE</sub> in 1 M KOH under simulated AM 1.5G solar irradiation.

As shown in Figure S12, the photocurrent density of Si/Al<sub>2</sub>O<sub>3</sub>/Ni photoanode drops sharply in a few hundred seconds, which is much lower than the 330 hours of the photoanode with NiFeO<sub>x</sub> film, indicating that the NiFeO<sub>x</sub> film is essential for obtaining high stability electrodes. Therefore, we can reasonably conclude that the NiFeO<sub>x</sub> film could effectively protect Si from corrosion during long operation.

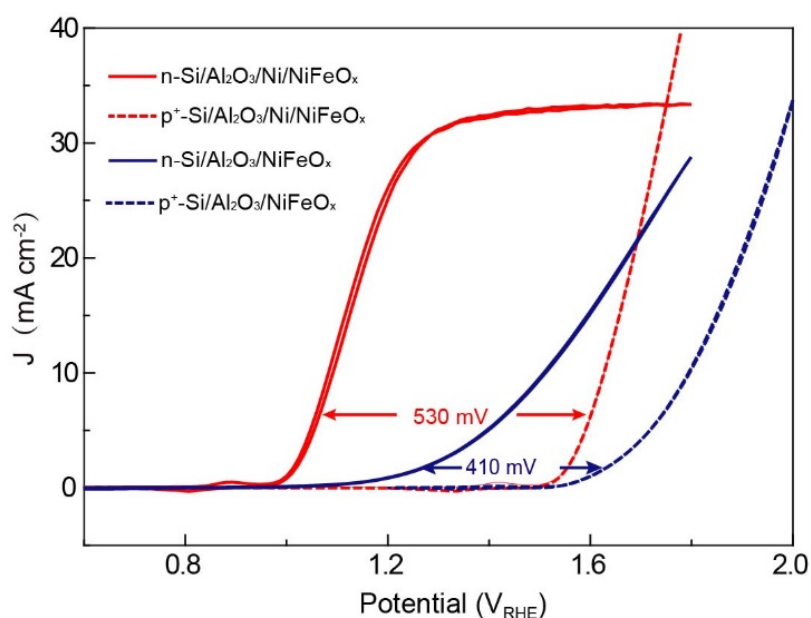


**Figure S13.** The J-V curves of the n-Si/Al<sub>2</sub>O<sub>3</sub>/Ni/NiFeO<sub>x</sub>, p<sup>+</sup>-Si/Al<sub>2</sub>O<sub>3</sub>/Ni/NiFeO<sub>x</sub>, n-Si/Al<sub>2</sub>O<sub>3</sub>/NiFeO<sub>x</sub> and p<sup>+</sup>-Si/Al<sub>2</sub>O<sub>3</sub>/Ni/NiFeO<sub>x</sub> photoanodes.

The photovoltages of the n-Si/Al<sub>2</sub>O<sub>3</sub>/Ni/NiFeO<sub>x</sub> and Si/Al<sub>2</sub>O<sub>3</sub>/NiFeO<sub>x</sub> photoanodes also were estimated by comparing the potential at 1 mA cm<sup>-2</sup> of the photoanode under illumination and the non-photoactive p<sup>+</sup>-Si/Al<sub>2</sub>O<sub>3</sub>/Ni/NiFeO<sub>x</sub> and p<sup>+</sup>-Si/Al<sub>2</sub>O<sub>3</sub>/NiFeO<sub>x</sub> (here the degenerate p<sup>+</sup>-Si simply acted as a conductive substrate),<sup>24</sup> and were measured to be 530 and 410 mV respectively, which is consistent with the measured photovoltage from OCP.

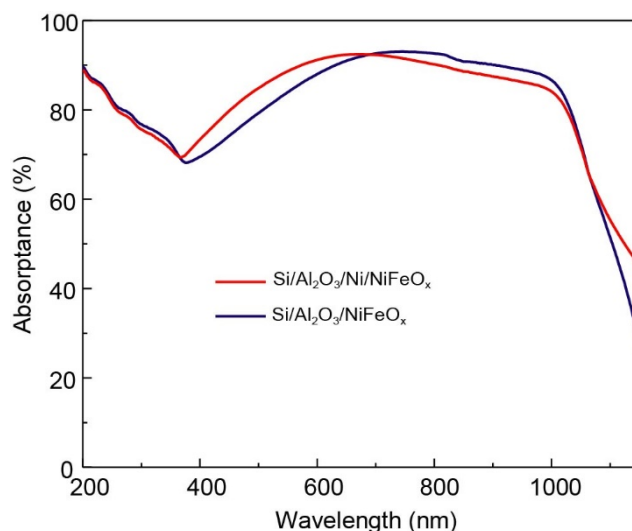


**Figure S14.** UV-visible absorbance spectra of the Si/Al<sub>2</sub>O<sub>3</sub>/Ni/NiFeO<sub>x</sub> and Si/Al<sub>2</sub>O<sub>3</sub>/NiFeO<sub>x</sub> photoanodes.

To evaluate the possible contribution of light absorption on the enhancement of the photocurrent density, UV-visible absorbance spectra of the two photoanodes were studied (Figure S14). The theoretical photocurrent densities of the photoanode with and without Ni film were calculated (by integrating the light absorbance for the solar spectrum), to be ~37.5 and ~37.2 mA cm<sup>-2</sup>, respectively.<sup>25</sup> This result indicates that the difference in light absorption between the two photoanodes is negligible.

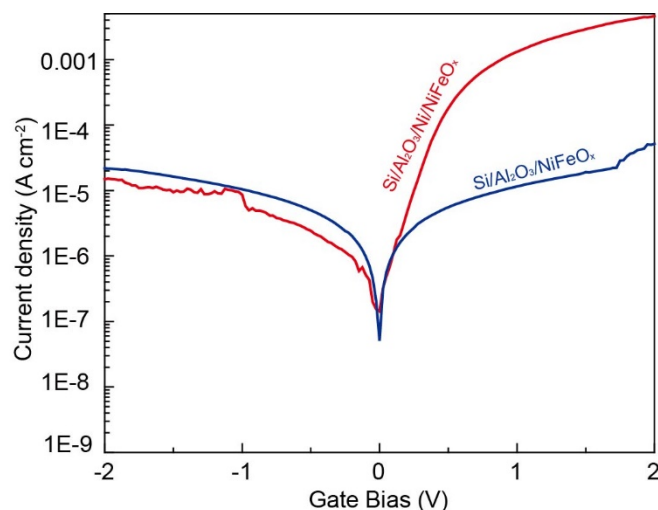


**Figure S15.** The solid-state device measurement of the Si/Al<sub>2</sub>O<sub>3</sub>/Ni/NiFeO<sub>x</sub> and Si/Al<sub>2</sub>O<sub>3</sub>/NiFeO<sub>x</sub>.

To analyze the reverse saturation current quantitatively as the reviewer suggested, the data fitting was performed using a single-diode model as shown in equation S13<sup>9</sup>:

$$j = j_0 \left[ \exp\left(\frac{q(V - R_s j)}{nkT}\right) \right] + \frac{V - R_s j}{R_p}$$

where  $j$  is the dark current density,  $j_0$  is the dark saturation current density,  $q$  is the elementary charge ( $1.6 \times 10^{-19}$  C),  $V$  is the gate bias,  $R_s$  is the series resistance,  $n$  is the ideality factor,  $k$  is the Boltzmann's constant ( $1.38 \times 10^{-23}$  J K<sup>-1</sup>),  $T$  is the temperature (293 K) and  $R_p$  is the parallel resistance. By fitting the measured dark current density-gate bias plot with equation S13, the obtained  $j_0$  of the Si/Al<sub>2</sub>O<sub>3</sub>/Ni/NiFeO<sub>x</sub> and Si/Al<sub>2</sub>O<sub>3</sub>/NiFeO<sub>x</sub> solid samples are  $3.4 \times 10^{-5}$  and  $5.5 \times 10^{-5}$  mA cm<sup>-2</sup> respectively. The lower reverse saturation current density of the Si/Al<sub>2</sub>O<sub>3</sub>/Ni/NiFeO<sub>x</sub> electrode implies the decrease in the surface state densities on the Si surface.

**Table S1.** The parameters with deviations extracted from the EIS measurements

	<b>Si/Al<sub>2</sub>O<sub>3</sub>/Ni/NiFeO<sub>x</sub></b>		<b>Si/Al<sub>2</sub>O<sub>3</sub>/ NiFeO<sub>x</sub></b>	
	<b>values</b>	<b>deviations</b>	<b>values</b>	<b>deviations</b>
R <sub>s</sub>	15.7	1.4%	16.4	3.6%
R <sub>1</sub>	11.1	3.5%	220.7	5.7%
CPE1-T	7.6×10 <sup>-7</sup>	40.4%	2.3×10 <sup>-7</sup>	17.0%
CPE1-R	0.89	3.6%	1.1	1.9%
R <sub>2</sub>	39.1	1.7%	176.9	5.7%
CPE2-T	6.8×10 <sup>-5</sup>	11.1%	3.4×10 <sup>-4</sup>	45.6%
CPE2-R	0.88	1.8%	0.4	8.4%

**Table S2.** Comparison of PEC performances n-Si photoanodes

(electrolyte is 1 M KOH unless otherwise specified)

<b>Photoanode</b>	<b>Onset potential (V<sub>RHE</sub>)</b>	<b>Current density at 1.23 V (mA cm<sup>-2</sup>)</b>	<b>Saturated current density (mA cm<sup>-2</sup>)</b>	<b>Stability</b>	<b>Reference</b>
n-Si/TiO <sub>2</sub> /Ir	1.03 (1 M NaOH)	8.89 (1 M NaOH)	Null	8 h (1 M NaOH)	26
n-Si/SiO <sub>2</sub> /Ni	1.07	11.76	54.7 (2 sun)	12 h	27
n-Si/TiO <sub>2</sub> /Ni	1.2	1	28.5	60 h	28
n-Si/NiO <sub>x</sub>	1.25	Null	30.7	686 h	14

n-Si/SiO <sub>x</sub> /CoO <sub>x</sub> /NiO <sub>x</sub>	0.98	28	30.8	1700 h	1
n-Si/NiSi <sub>x</sub> /NiO <sub>x</sub> -annealed/Au NPs	0.88	34	37.03	10	29
n-Si/SiO <sub>x</sub> /CoO <sub>x</sub>	1.02	23.2	30.2	2500 h	30
n-Si//TiO <sub>x</sub> /ITO/NiOOH	0.9	18	40	6.7 h (1 M LiOH)	31
n-Si/SiO <sub>x</sub> /Al <sub>2</sub> O <sub>3</sub> /Pt/Ni	1.0	19.2	28.5	200 h	6
n-Si/SiO <sub>x</sub> /Ni@Ni(OH) <sub>2</sub>	1.03	15.5	36.4	300 h (KCl, pH 9)	32
Si/SiO <sub>x</sub> /Ni@Co	1.02	10.65	36.7	100 h (KCl, pH 9)	33
n-Si/Ni/NiO <sub>x</sub>	1.08	14.7	31.7	6.9 h (1 M NaOH)	3
n-Si/Al <sub>2</sub> O <sub>3</sub> /Ni/NiO <sub>x</sub> /NiOOH	0.85	28	32	80 h	34
n-Si/ZrO <sub>2</sub> /NiFe	0.96	26.6	36.4	100 h	35
n-Si/SiO <sub>x</sub> /SnO <sub>x</sub> /Ni	0.91	30.8	31.5	25 h	36
n-Si/Al <sub>2</sub> O <sub>3</sub> /Ni/NiFeO <sub>x</sub> /NiFe-LDH	0.92	31	33.5	330 h	our work

## References

- (1) Zhou, X.; Liu, R.; Sun, K.; Friedrich, D.; McDowell, M. T.; Yang, F.; Omelchenko, S. T.; Saadi, F. H.; Nielander, A. C.; Yalamanchili, S.; Papadantonakis, K. M.; Brunschwig, B. S.; Lewis, N. S., Interface Engineering of the Photoelectrochemical Performance of Ni-Oxide-Coated n-Si Photoanodes by Atomic-Layer Deposition of Ultrathin Films of Cobalt Oxide. *Energy Environ. Sci.* **2015**, 8 (9), 2644-2649.
- (2) Sun, K.; Saadi, F. H.; Lichterman, M. F.; Hale, W. G.; Wang, H.-P.; Zhou, X.; Plymale, N. T.; Omelchenko, S. T.; He, J.-H.; Papadantonakis, K. M.; Brunschwig, B. S.; Lewis, N. S., Stable Solar-Driven Oxidation of Water by Semiconducting Photoanodes Protected by Transparent Catalytic Nickel Oxide Films. *Proc. Natl. Acad. Sci. U.S.A.* **2015**, 112 (12), 3612-3617.
- (3) Lee, S. A.; Lee, T. H.; Kim, C.; Lee, M. G.; Choi, M.-J.; Park, H.; Choi, S.; Oh, J.; Jang, H. W., Tailored NiO<sub>x</sub>/Ni Cocatalysts on Silicon for Highly Efficient Water Splitting Photoanodes Via Pulsed Electrodeposition. *ACS Catal.* **2018**, 8 (8), 7261-7269.
- (4) Guo, B.; Batool, A.; Xie, G.; Boddula, R.; Tian, L.; Jan, S. U.; Gong, J. R., Facile Integration between Si and Catalyst for High-Performance Photoanodes by a Multifunctional Bridging Layer. *Nano Lett.* **2018**, 18 (2), 1516-1521.
- (5) Yu, X.; Yang, P.; Chen, S.; Zhang, M.; Shi, G., NiFe Alloy Protected Silicon Photoanode for Efficient Water Splitting. *Adv. Energy Mater.* **2017**, 7 (6), 1601805.
- (6) Digdaya, I. A.; Adhyaksa, G. W. P.; Trześniewski, B. J.; Garnett, E. C.; Smith, W. A., Interfacial Engineering of Metal-Insulator-Semiconductor Junctions for Efficient and Stable Photoelectrochemical Water Oxidation. *Nat. Commun.* **2017**, 8, 15968.
- (7) Hemmerling, J.; Quinn, J.; Linic, S., Quantifying Losses and Assessing the Photovoltage Limits in Metal–Insulator–Semiconductor Water Splitting Systems. *Adv. Energy Mater.* **2020**, 10 (12), 1903354.

- (8) Al-Shankiti, I. A.; Bayon, A.; Weimer, A. W., Reduction Kinetics of Hercynite Redox Materials for Solar Thermochemical Water Splitting. *Chem. Eng. J.* **2020**, 389, 124429.
- (9) Digdaya, I. A.; Trzesniewski, B. J.; Adhyaksa, G. W. P.; Garnett, E. C.; Smith, W. A., General Considerations for Improving Photovoltage in Metal-Insulator-Semiconductor Photoanodes. *J. Phys. Chem. C* **2018**, 122 (10), 5462-5471.
- (10) Hill, J. C.; Landers, A. T.; Switzer, J. A., An Electrodeposited Inhomogeneous Metal-Insulator-Semiconductor Junction for Efficient Photoelectrochemical Water Oxidation. *Nat. Mater.* **2015**, 14 (11), 1150-1155.
- (11) Quinn, J.; Hemmerling, J.; Linic, S., Maximizing Solar Water Splitting Performance by Nanoscopic Control of the Charge Carrier Fluxes across Semiconductor-Electrocatalyst Junctions. *ACS Catal.* **2018**, 8 (9), 8545-8552.
- (12) Zheng, J.; Lyu, Y.; Xie, C.; Wang, R.; Tao, L.; Wu, H.; Zhou, H.; Jiang, S.; Wang, S., Defect-Enhanced Charge Separation and Transfer within Protection Layer/Semiconductor Structure of Photoanodes. *Adv. Mater.* **2018**, 30 (31), 1801773.
- (13) Sun, K.; Pang, X.; Shen, S.; Qian, X.; Cheung, J. S.; Wang, D., Metal Oxide Composite Enabled Nanotextured Si Photoanode for Efficient Solar Driven Water Oxidation. *Nano Lett.* **2013**, 13 (5), 2064-2072.
- (14) Sun, K.; McDowell, M. T.; Nielander, A. C.; Hu, S.; Shaner, M. R.; Yang, F.; Brunschwig, B. S.; Lewis, N. S., Stable Solar-Driven Water Oxidation to O<sub>2</sub>(g) by Ni-Oxide-Coated Silicon Photoanodes. *J. Phys. Chem. Lett.* **2015**, 6 (4), 592-598.
- (15) Lawrence Salvat, J.; E.Makovsky, L.; Stencel, J. M.; Brown, F. R.; Hercules, D. M., Surface Spectroscopic Study of Tungsten-Alumina Catalysts Using X-Ray Photoelectron, Ion Scattering, and Raman Spectroscopies. *J. Phys. Chem.* **1981**, 85 (24), 3700-3707.
- (16) Wu, G.; Chen, W.; Zheng, X.; He, D.; Luo, Y.; Wang, X.; Yang, J.; Wu, Y.; Yan, W.; Zhuang, Z.; Hong, X.; Li, Y., Hierarchical Fe-Doped NiO<sub>x</sub> Nanotubes Assembled from



Ultrathin Nanosheets Containing Trivalent Nickel for Oxygen Evolution Reaction. *Nano Energy* **2017**, 38, 167-174.

(17) Yamashita, T.; Hayes, P., Analysis of XPS Spectra of Fe<sup>2+</sup> and Fe<sup>3+</sup> Ions in Oxide Materials. *Appl. Surf. Sci.* **2008**, 254 (8), 2441-2449.

(18) Hsua, C.-Y.; Chen, W.-T.; Chen, Y.-C.; Weib, H.-Y.; Yen, Y.-S.; Huang, K.-C.; Hob, K.-C.; Chu, C.-W.; Lin, J. T., Charge Transporting Enhancement of NiO Photocathodes for p-Type Dye-Sensitized Solar Cells. *Electrochim. Acta* **2012**, 66, 210-215.

(19) Papaderakis, A.; Pliatsikas, N.; Prochaska, C.; Papazisi, K. M.; Balomenou, S. P.; Tsiplakides, D.; Patsalas, P.; Sotiropoulos, S., Ternary Pt-Ru-Ni Catalytic Layers for Methanol Electrooxidation Prepared by Electrodeposition and Galvanic Replacement. *Front. Chem.* **2014**, 2, 29.

(20) Zhang, F.; Zhu, D.; Chen, X. a.; Xu, X.; Yang, Z.; Chao Zou; Yang, K.; Huang, S., A Nickel Hydroxide-Coated 3D Porous Graphene Hollow Sphere Framework as a High Performance Electrode Material for Supercapacitors. *Phys. Chem. Chem. Phys.* **2014**, 16 (9), 4186-92.

(21) Britto, R. J.; Benck, J. D.; Young, J. L.; Hahn, C.; Deutsch, T. G.; Jaramillo, T. F., Molybdenum Disulfide as a Protection Layer and Catalyst for Gallium Indium Phosphide Solar Water Splitting Photocathodes. *J. Phys. Chem. Lett.* **2016**, 7 (11), 2044-9.

(22) Back-Illuminated Si-Based Photoanode with Nickel Cobalt Oxide Catalytic Protection Layer. *ChemElectroChem* **2016**, 3 (10), 1546-1552.

(23) He, L.; Zhou, W.; Cai, D.; Mao, S. S.; Sun, K.; Shen, S., Pulsed Laser-Deposited n-Si/NiO<sub>x</sub> Photoanodes for Stable and Efficient Photoelectrochemical Water Splitting. *Catal. Sci. Technol.* **2017**, 7 (12), 2632-2638.

(24) Scheuermann, A. G.; Chidsey, C. E. D.; McIntyre, P. C., Understanding Photovoltage in Insulator-Protected Water Oxidation Half-Cells. *J. Electrochem. Soc.* **2015**, 163 (3), 192-200.

- (25) Guo, B.; Tian, L.; Xie, W.; Batool, A.; Xie, G.; Xiang, Q.; Jan, S. U.; Boddula, R.; Gong, J. R., Vertically Aligned Porous Organic Semiconductor Nanorod Array Photoanodes for Efficient Charge Utilization. *Nano Lett.* **2018**, *18* (9), 5954-5960.
- (26) Chen, Y. W.; Prange, J. D.; Dühnen, S.; Park, Y.; Gunji, M.; Chidsey, C. E. D.; McIntyre, P. C., Atomic Layer-Deposited Tunnel Oxide Stabilizes Silicon Photoanodes for Water Oxidation. *Nat. Mater.* **2011**, *10* (7), 539-544.
- (27) Kenney, M. J.; Gong, M.; Li, Y.; Wu, J. Z.; Feng, J.; Lanza, M.; Dai, H., High-Performance Silicon Photoanodes Passivated with Ultrathin Nickel Films for Water Oxidation. *Science* **2013**, *342* (6160), 836-840.
- (28) McDowell, M. T.; Lichterman, M. F.; Carim, A. I.; Liu, R.; Hu, S.; Brunschwig, B. S.; Lewis, N. S., The Influence of Structure and Processing on the Behavior of TiO<sub>2</sub> Protective Layers for Stabilization of n-Si/TiO<sub>2</sub>/Ni Photoanodes for Water Oxidation. *ACS Appl. Mater. Interfaces* **2015**, *7* (28), 15189-15199.
- (29) Ying, Z.; Yang, X.; Tong, R.; Zhu, Q.; Chen, T.; He, Z.; Pan, H., Enhancing the Efficiency and Stability of NiO<sub>x</sub>-Based Silicon Photoanode Via Interfacial Engineering. *ACS Appl. Energy Mater.* **2019**, *2* (9), 6883-6890.
- (30) Zhou, X.; Liu, R.; Sun, K.; Papadantonakis, K. M.; Brunschwig, B. S.; Lewis, N. S., 570 mV Photovoltage, Stabilized n-Si/CoO<sub>x</sub> Heterojunction Photoanodes Fabricated Using Atomic Layer Deposition. *Energy Environ. Sci.* **2016**, *9* (3), 892-897.
- (31) Yao, T.; Che, R.; Li, J.; Han, J.; Qin, W.; Wang, H.; Shi, J.; Fan, F.; Li, C., Manipulating the Interfacial Energetics of n-Type Silicon Photoanode for Efficient Water Oxidation. *J. Am. Chem. Soc.* **2016**, *138* (41), 13664-13672.
- (32) Xu, G.; Xu, Z.; Shi, Z.; Pei, L.; Yan, S.; Gu, Z.; Zou, Z., Silicon Photoanodes Partially Covered by Ni@Ni(OH)<sub>2</sub> Core-Shell Particles for Photoelectrochemical Water Oxidation. *ChemSusChem* **2017**, *10* (14), 2897-2903.

- (33) Chen, J.; Xu, G.; Wang, C.; Zhu, K.; Wang, H.; Yan, S.; Yu, Z.; Zou, Z., High-Performance and Stable Silicon Photoanode Modified by Crystalline Ni@Amorphous Co Core-Shell Nanoparticles. *ChemCatChem* **2018**, *10* (21), 5025-5031.
- (34) Luo, Z.; Liu, B.; Li, H.; Chang, X.; Zhu, W.; Wang, T.; Gong, J., Multifunctional Nickel Film Protected n-Type Silicon Photoanode with High Photovoltage for Efficient and Stable Oxygen Evolution Reaction. *Small Methods* **2019**, 1900212.
- (35) Cai, Q.; Hong, W.; Jian, C.; Li, J.; Liu, W., Insulator Layer Engineering toward Stable Si Photoanode for Efficient Water Oxidation. *ACS Catal.* **2018**, *8* (10), 9238-9244.
- (36) Moreno-Hernandez, I. A.; Brunschwig, B. S.; Lewis, N. S., Tin Oxide as a Protective Heterojunction with Silicon for Efficient Photoelectrochemical Water Oxidation in Strongly Acidic or Alkaline Electrolytes. *Adv. Energy Mater.* **2018**, *8* (24), 1801155.